Structure, Volume *24*

Supplemental Information

Acoustic Injectors for Drop-On-Demand Serial Femtosecond Crystallography

Christian G. Roessler, Rakhi Agarwal, Marc Allaire, Roberto Alonso-Mori, Babak Andi, José F.R. Bachega, Martin Bommer, Aaron S. Brewster, Michael C. Browne, Ruchira Chatterjee, Eunsun Cho, Aina E. Cohen, Matthew Cowan, Sammy Datwani, Victor L. Davidson, Jim Defever, Brent Eaton, Richard Ellson, Yiping Feng, Lucien P. Ghislain, James M. Glownia, Guangye Han, Johan Hattne, Julia Hellmich, Annie Héroux, Mohamed Ibrahim, Jan Kern, Anthony Kuczewski, Henrik T. Lemke, Pinghua Liu, Lars Majlof, William M. McClintock, Stuart Myers, Silke Nelsen, Joe Olechno, Allen M. Orville, Nicholas K. Sauter, Alexei S. Soares, S. Michael Soltis, Heng Song, Richard G. Stearns, Rosalie Tran, Yingssu Tsai, Monarin Uervirojnangkoorn, Carrie M. Wilmot, Vittal Yachandra, Junko Yano, Erik T. Yukl, Diling Zhu, and Athina Zouni

Supplemental Data and Supplemental Experimental Procedures

Acoustic injectors for drop-on-demand serial femtosecond crystallography

Christian G. Roessler[1], Rakhi Agarwal[2, 14], Marc Allaire[1,16,*], Roberto Alonso-Mori[9], Babak Andi[1], José F. R. Bachega[5], Martin Bommer[13], Aaron S. Brewster[3], Michael C. Browne[9], Ruchira Chatterjee[3], Eunsun Cho[4], Aina E. Cohen[11], Matthew Cowan[1], Sammy Datwani[6], Victor L. Davidson[8], Jim Defever[9], Brent Eaton[6], Richard Ellson[6], Yiping Feng[9], Lucien P. Ghislain[6], James M. Glownia[9], Guangye Han[3], Johan Hattne[3,17], Julia Hellmich[12,13], Annie Héroux[1], Mohamed Ibrahim[13], Jan Kern[3,9], Anthony Kuczewski[1], Henrik T. Lemke[9,18], Pinghua Liu[4], Lars Majlof[6], William M. McClintock[6], Stuart Myers[1], Silke Nelsen[9], Joe Olechno[6], Allen M. Orville[1,2,19,*], Nicholas K. Sauter[3], Alexei S. Soares[1,*], S. Michael Soltis[11], Heng Song[4], Richard G. Stearns[6], Rosalie Tran[3], Yingssu Tsai[9,10], Monarin Uervirojnangkoorn[3], Carrie M. Wilmot[7], Vittal Yachandra[3], Junko Yano[3], Erik T. Yukl[7,15], Diling Zhu[9], Athina Zouni[13]

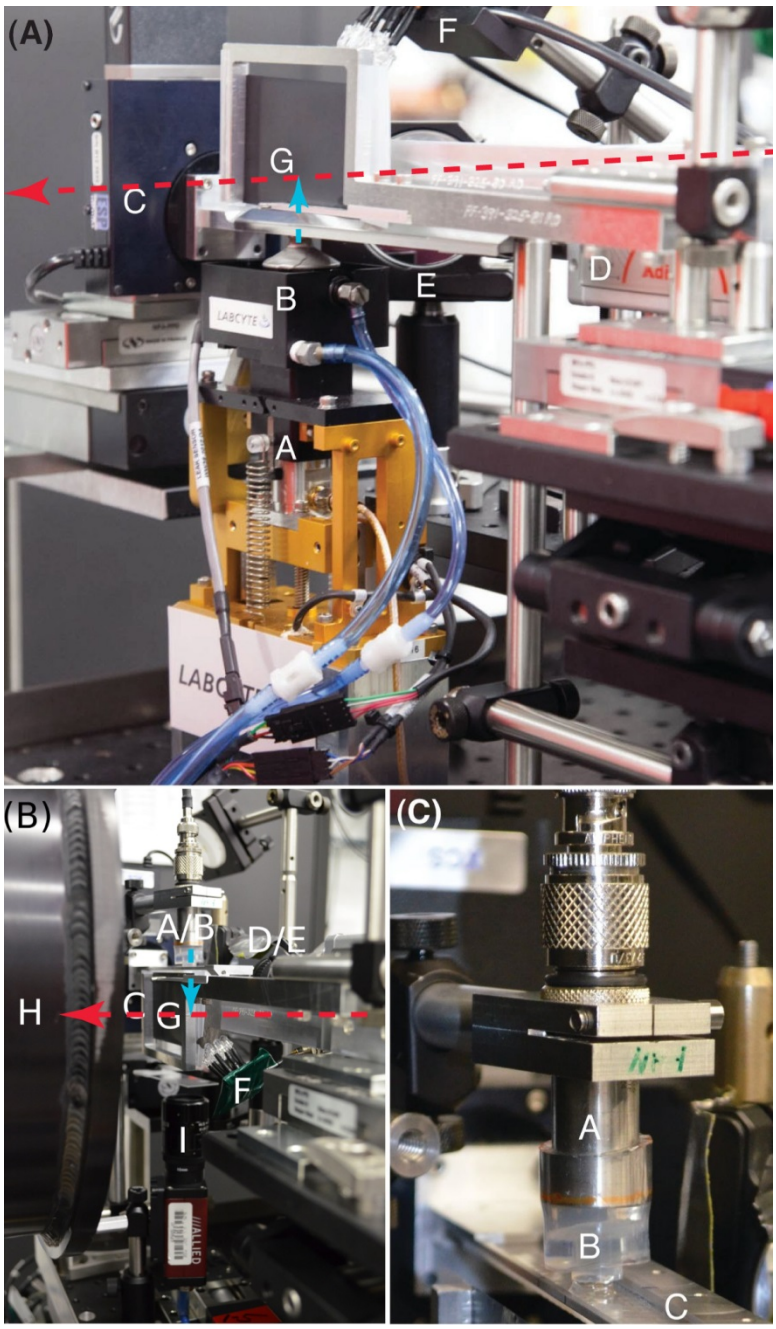

Figure S1, related to Figure 1: Acoustic injection experimental setups at the LCLS XPP instrument: acoustic transducer assembly for modified Echo and inverted systems. *(A)* Modified Echo setup. Components include A) the transducer assembly, B) the flowing water coupling system, C) goniometer for the sample tray (aluminum holder extending horizontally to the right), D) off-axis infrared camera to view on-axis droplets, E) 45° mirror with a center hole for on-axis visualization, F) stroboscopic LED array, G) X-ray transparent stroboscopic reflection film. The X-ray beam comes in from the center right of the image (red dashed arrow) and droplets are injected upward (blue dashed arrow), for reference. *(B)* Inverted system. Components include A) and B) Transducer and agarose coupling column, and C) through G) the same components listed in the Modified Echo setup. H) the CSPAD X-ray detector located about 100 mm from the interaction zone. I) camera and optics to visualize ejected droplets falling onto a coverslip. The X-ray beam comes in from the right center right of the image (red dashed arrow) and the droplets are injected downward (blue dashed arrow), for reference. *(C)* A close-up of the inverted setup in *(B)*. A) the transducer, B) the agarose coupling column contained in plastic tubing, and C) the sample holder. Image in panel (*A*) courtesy of Brad Plummer, SLAC.

Figure S2A, related to Figure 2: Example radial intensity plot versus angle calculated from a single diffraction image and used for water scatter analysis and droplet hit classification. The shaded rectangle indicates the region where the water peak appears. Intensity is measured in analog-to-digital units (ADUs).

Figure S2B: SFX data collected at ambient conditions displays low mosaic spread. Histogram of Bragg reflection sizes (in number of pixels) for diffraction images from five experimental runs on Lysozyme samples.

A.

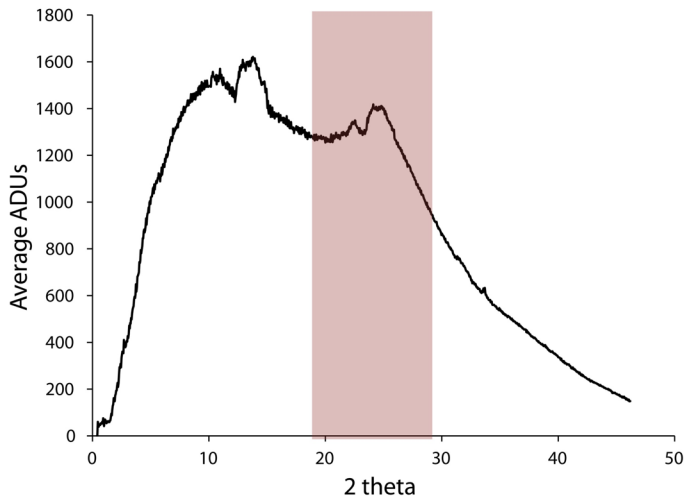

B.

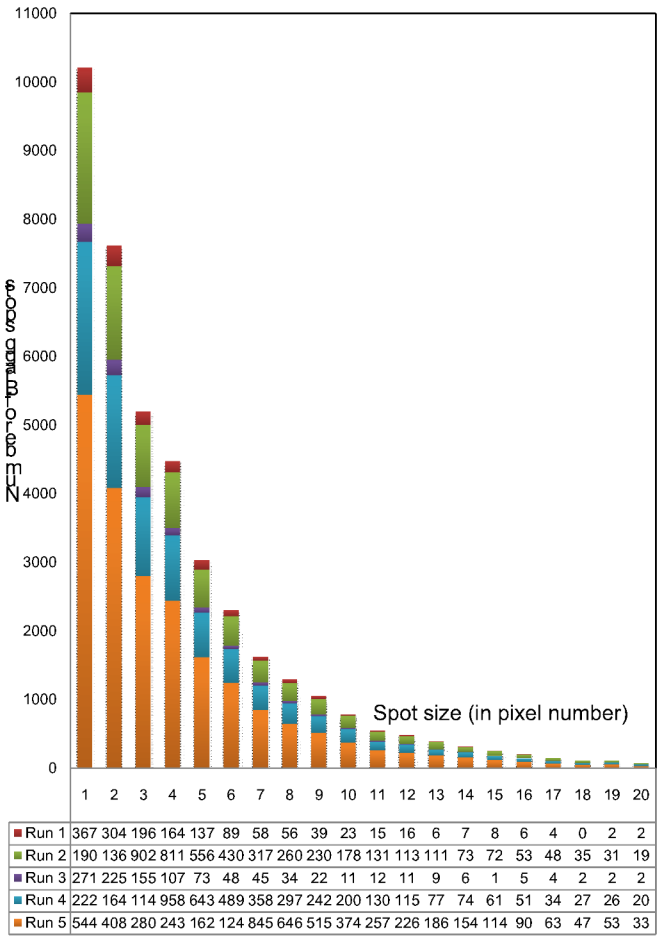

Figure S3, related to Figure 3: An example of the quality of the electron density maps for the structure of lysozyme. The 2 $F_o - F_c$ map to 2.13 Å resolution is contoured at 1.5 σ. Atoms are colored green, red, blue, and orange for C, O, N, and S, respectively.

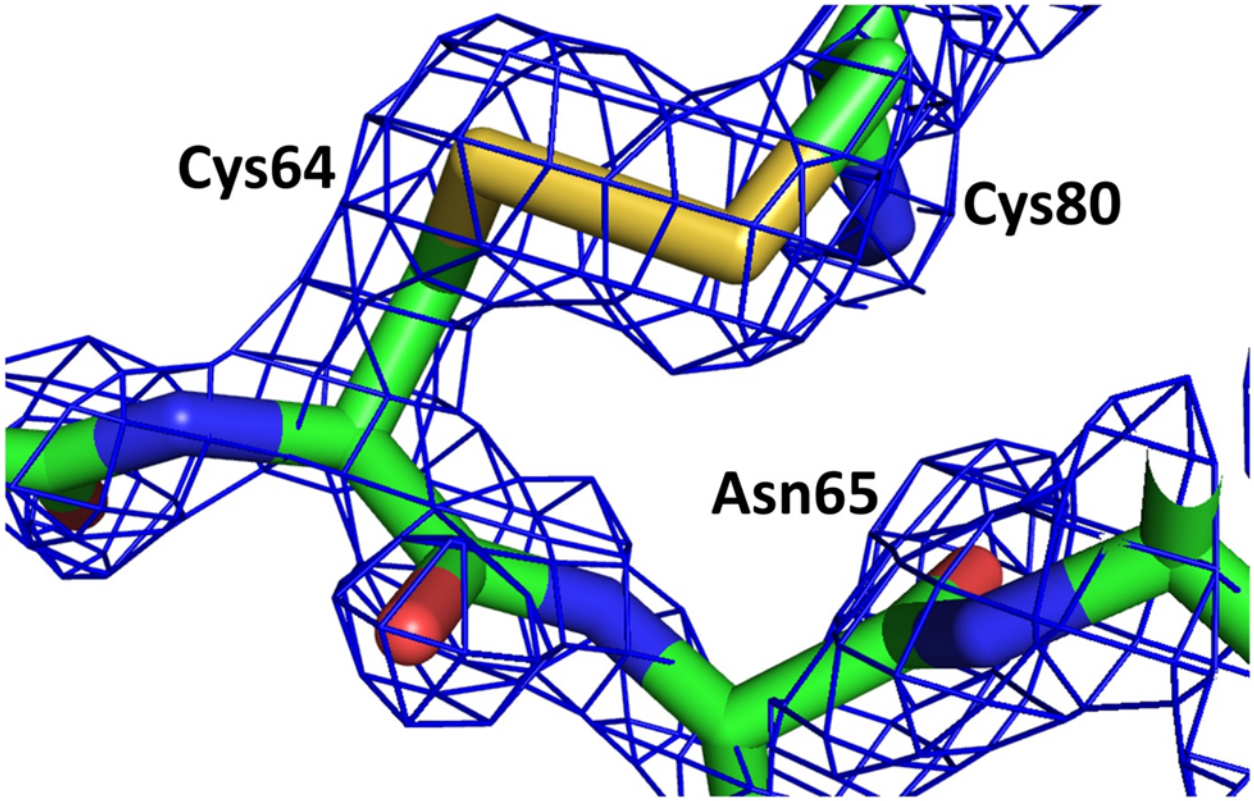

Table S1 related to Figure 1. Selected Sample and Injector Characteristics,

Sample	Major precipitant	Space group	Cell dimensions (Å and degrees)	Solvent content (%)	Distribution of crystal sizes and morphologies	Acoustic injector parameters 15 MHz transducer, 0.4 V waveform amplitude			
						Burst count	Burst length (µs)	Coupler Vf (V, pp)	Coupler Vr (V, pp)
Water	na	na	na	100	na	2,100	173	5.2	2.8
MauG•MADH	22 - 26% (w/v) PEG 8000	C2	346 × 55 × 112; 90, 107, 90	53	Plates, 10-50 µm; longest dimension	6,500	433		3.76
Stc2, ES	2.5 - 10% (w/v) PEG 3350, 10% glycerol	$P6_322$	97 × 97 × 178; 90, 90, 120	62	polyhedra; 25-50 µm	2,500	167	5.2	2.96
Stc2, E*	2.5 - 10% (w/v) PEG 3350, 10% glycerol	$P6_322$	97 × 97 × 178; 90, 90, 120	62	polyhedra; 50-100 µm	2,500	167	5.2	2.96
Stc2, E*S	2.5 - 10% (w/v) PEG 3350, 10% glycerol	$P6_322$	97 × 97 × 178; 90, 90, 120	62	polyhedra; 200-300 µm	2,500	167	5.04	2.96
Thermolysin	15% (w/v) $(NH_4)_2SO_4$	$P6_122$	93 × 93 × 130; 90, 90, 120	47	10-100 µm	1,900	127	5.2	2.96
Lysozyme	8% (w/v) sodium chloride, 10% (v/v) ethylene glycol	$P4_32_12$	78 × 78 × 37; 90, 90, 90	38	5-100 µm	1,900	127	5.2	2.96
oxy-HbGp	1.6 M K_2HPO_4	I222	273 × 320 × 333; 90, 90, 90	70-71	Plates, 50-250 µm; longest dimension	1,900	127	5.2	2.96
PS II (PEG 2,000)	8 - 10% (w/v) PEG 2000	$P2_12_12_1$	132 × 227 × 307; 90, 90, 90	67	50-400 µm, sorted into either 50-100 µm or > 150 µm groups	5,100	340	5.2	
PS II (PEG 5,000)	40% (w/v) PEG 5000, 100 mM $(NH_4)_2SO_4$	$P2_12_12_1$	115 × 220 × 303; 90, 90, 90	61	polyhedra; 50-100 µm	10,500	700		3.76

Coupler Vf, forward voltage in Volts peak to peak

Coupler Vr, reverse voltage in Volts peak to peak

Table S2 related to Figures 2 and 3 and Table S1. Stachydrine demethylase data processing and refinement statistics

Stachydrine demethylase (Stc2) merging statistics by resolution bin									
Resolution Range	**# Lattices**	**# Measurements**	**# Unique reflections**	**Completeness (%)**	**<Multiplicity>**	**<I/σ(I)>**	**$CC_{1/2}$ (%)**	**CC_{iso} (%)**	**R_{split}(%)**
∞ - 4.39	2,796	394,995	3,587	99.4	110.1	40.9	76.2%	77.1%	36.2%
4.39 - 3.48	2,696	362,648	3,375	100.0	107.5	33.5	69.6%	76.5%	36.6%
3.48 - 3.04	2,446	228,883	3,311	100.0	69.1	19.1	58.2%	59.0%	42.6%
3.04 - 2.76	1,898	172,917	3,315	100.0	52.2	12.9	50.5%	53.1%	47.3%
2.76 - 2.57	1,457	120,306	3,257	100.0	36.9	8.8	40.2%	33.9%	51.0%
2.57 - 2.42	1,093	77,222	3,269	100.0	23.6	6.2	26.4%	36.6%	59.7%
2.42 - 2.29	777	48,015	3,253	100.0	14.8	4.6	16.5%	26.6%	68.5%
2.29 - 2.19	551	32,783	3,235	99.9	10.1	3.7	8.3%	13.2%	76.9%
∞ - 2.19	2,796	1,437,769	26,602	99.9	53.6	16.5	80.8%	75.4%	43.1%
2.19 - 2.11	381	22,032	3,230	99.3	6.8	2.8	6.6%	15.0%	87.5%
2.11 - 2.04	250	11,980	3,081	96.5	3.9	2.0	10.7%	4.2%	90.6%
2.04 - 1.97	146	4,879	2,401	74.0	2.0	1.5	14.1%	20.2%	90.7%
1.97 - 1.92	72	1,801	1,320	41.2	1.4	1.3	11.4%	11.6%	96.6%
1.92 - 1.87	34	643	554	17.1	1.2	1.1	13.6%	94.8%	93.3%
1.87 - 1.82	11	152	148	4.6	1.0	1.2	n.a.	n.a.	n.a.
1.82 - 1.78	4	19	19	0.6	1.0	1.1	n.a.	n.a.	n.a.
∞ - 1.78	2,796	1,479,275	37,355	75.5	39.6	12.4	78.5%	75.4%	46.4%

Stachydrine demethylase (Stc2) maximum likelihood refinement with Refmac 5.8.0069						
Space Group	$P6_3$ 2 2					
Unit Cell (Å and degrees)	a = 98.4	b = 98.4	c = 180.1	α = 90	β = 90	γ = 120
Resolution range (Å)	90	2.2				
High resolution shell (Å)	2.26	2.2				
No. reflections / test set	26876	1292				
Rwork / Rfree	0.269	0.33				
Rwork / Rfree (high resolution shell)	0.426	0.511				
No. atoms	3306					
No. protein atoms	3159					
No. hetatoms (water, Rieske cluster, Fe(II))	134	4	1			
B-factors ($Å^2$)						
Wilson B, protein	21.38					
B-value, (water, Rieske cluster, Fe(II))	17.12	12.14	52.72			
R.m.s. deviations						
Bonds lengths (Å)	0.013					
Bond angles (degrees)	1.766					
Chiral volume	0.093					

Table S3 related to Figures 2 and S3 and Table S1. Lysozyme data processing and refinement statistics

Lysozyme merging statistics by resolution bin

Resolution Range	# Lattices	# Measurements	# Unique reflections	Completeness (%)	<Multiplicity>	<I/σ(I)>	$CC_{1/2}$ (%)	CC_{iso} (%)	R_{split}(%)
∞ - 4.07	558	27,941	1,110	99.6	25.2	32.9	30.7%	70.0%	62.0%
4.07 - 3.23	553	22,738	1,032	100.0	22.0	24.8	39.5%	69.9%	60.6%
3.23 - 2.82	528	18,935	1,015	100.0	18.7	14.9	30.7%	64.9%	72.4%
2.82 - 2.56	486	15,516	1,004	100.0	15.5	10.4	27.2%	55.4%	71.4%
2.56 - 2.38	437	10,657	990	99.9	10.8	7.1	15.0%	47.5%	79.2%
2.38 - 2.24	370	8,866	996	99.8	8.9	6.2	8.1%	41.3%	86.8%
2.24 - 2.13	326	7,422	996	99.7	7.5	4.5	11.1%	40.7%	86.4%
∞ - 2.13	558	112,075	7,143	99.8	15.6	14.7	42.0%	77.7%	69.3%
2.13 - 2.03	264	4,814	974	98.7	4.9	3.5	2.2%	17.4%	94.0%
2.03 - 1.95	204	2,537	881	88.8	2.9	2.7	1.1%	19.0%	98.1%
1.95 - 1.89	144	1,178	659	67.1	1.8	2.2	3.8%	16.8%	98.2%
1.89 - 1.83	99	578	433	44.5	1.3	1.7	2.1%	n.a.	97.4%
1.83 - 1.78	61	199	180	18.2	1.1	1.7	53.7%	n.a.	65.2%
1.78 - 1.73	29	52	50	5.2	1.0	2.3	100.0%	n.a.	44.1%
1.73 - 1.69	9	21	21	2.2	1.0	1.8	n.a.	n.a.	n.a.
1.69 - 1.65	4	5	5	0.5	1.0	1.2	n.a.	n.a.	n.a.
∞ - 1.65	558	121,459	10,346	68.3	11.7	11.0	36.5%	67.1%	73.4%

Lysozyme maximum likelihood refinement with Refmac 5.8.0069

Space Group	$P4_3\,2_1\,2$					
Unit Cell (Å and degrees)	a = 75.5	b = 75.5	c = 37.6	α = 90	β = 90	γ = 90
Resolution range (Å)	55.5	2.13				
High resolution shell (Å)	2.19	2.13				
No. reflections / test set	6590	361				
Rwork / Rfree	0.242	0.333				
Rwork / Rfree (high resolution shell)	0.323	0.448				
No. atoms	1161					
No. protein atoms	1001					
No. hetatoms (water, Na^+, Cl^-)	160	1	5			
B-factors (Å^2)						
Wilson B, protein	16.49					
B-value, (water, Na+, Cl^-)	20.2	32.32	32.11			
R.m.s. deviations						
Bonds lengths (Å)	0.012					
Bond angles (degrees)	1.603					
Chiral volume	0.091					

Table S4 related to Figure 2 and Table S1. Thermolysin data processing and refinement statistics

Thermolysin merging statistics by resolution bin

Resolution Range	# Lattices	# Measurements	# Unique reflections	Completeness (%)	<Multiplicity>	<I/σ(I)>	$CC_{1/2}$ (%)	CC_{iso} (%)	R_{split}(%)
∞ - 4.32	916	90,164	2,563	99.6	35.2	21.1	46.0%	61.6%	56.1%
4.32 - 3.43	908	70,684	2,405	100.0	29.4	15.6	37.3%	61.8%	58.4%
3.43 - 2.99	855	45,179	2,382	100.0	19.0	8.9	31.6%	64.3%	63.0%
2.99 - 2.72	741	37,481	2,363	100.0	15.9	6.2	26.8%	56.3%	66.4%
2.72 - 2.52	597	24,167	2,331	99.9	10.4	4.4	15.5%	46.9%	70.1%
∞ - 2.52	916	267,675	12,044	99.9	22.0	11.3	46.4%	66.9%	60.2%
2.52 - 2.38	460	16,766	2,313	99.6	7.3	3.1	9.4%	44.3%	75.1%
2.38 - 2.26	338	12,486	2,286	98.5	5.5	2.6	8.2%	35.2%	78.0%
2.26 - 2.16	249	9,186	2,235	96.7	4.1	2.1	7.6%	26.0%	83.2%
2.16 - 2.07	172	5,112	2,011	87.3	2.5	1.6	12.1%	21.0%	89.5%
2.07 - 2.00	109	2,504	1,441	62.6	1.7	1.2	1.7%	14.9%	90.1%
2.00 - 1.94	64	873	711	31.0	1.2	1.2	n.a.	11.9%	94.5%
1.94 - 1.89	34	407	384	16.7	1.1	1.0	n.a.	35.4%	82.1%
1.89 - 1.84	20	133	129	5.6	1.0	0.9	n.a.	n.a.	55.7%
1.84 - 1.79	11	44	43	1.9	1.0	0.9	n.a.	n.a.	n.a.
1.79 - 1.75	2	4	4	0.2	1.0	0.8	n.a.	n.a.	n.a.
∞ - 1.75	916	315,190	23,601	66.6	13.4	6.9	48.6%	69.9%	63.9%

Thermolysin maximum likelihood refinement with Refmac 5.8.0069

Space Group	$P6_1$ 2 2					
Unit Cell (Å and degrees)	a = 92.7	b = 92.7	c = 129.5	α = 90	β = 90	γ = 120
Resolution range (Å)	80.3	2.52				
High resolution shell (Å)	2.59	2.52				
No. reflections / test set	11101	564				
Rwork / Rfree	0.222	0.288				
Rwork / Rfree (high resolution shell)	0.268	0.341				
No. atoms	2706					
No. protein atoms	2431					
No. hetatoms (water, Ca^{2+}, Zn^{2+})	269	5	1			
B-factors (Å^2)						
Wilson B, protein	18.163					
B-value, (water, Ca^{2+}, Zn^{2+})	12.422	21.55	3.86			
R.m.s. deviations						
Bonds lengths (Å)	0.012					
Bond angles (degrees)	1.586					
Chiral volume	0.087					

Supplemental Experimental Procedures

Cloning, expression, and purification of giant hemoglobin, PS II, MauG·MADH, and Stc2. Purified oxygen-bound giant extracellular hemoglobin (oxy-HbGp) was isolated directly from adult *Glossoscolex paulistus* as previously described (Agustinho et al., 1996; Bachega et al., 2011; Royer et al., 2006). PS II was isolated from *Thermosynechococcus elongatus* and purified as previously reported (Kern et al., 2005). MauG and MADH were expressed and purified as previously reported (Davidson, 1990; Wang et al., 2003). Active Stc2 was expressed and purified anaerobically as previously described (Daughtry et al., 2012). Stc2 was also expressed from a N-terminal His_6-tag construct provided by Dr. Ronald D. Seidel and Dr. Mark B. Stead. This purification differed from published procedures in that bacterial cell lysate containing His6-Stc2 (E*) was first applied to a Ni-NTA column followed by a Superdex 200 column, both under aerobic conditions (Agarwal, unpublished data).

Crystallization. Chemical reagents were purchased from Sigma-Aldrich (St. Louis, MO, USA) unless otherwise specified. Lyophilized thermolysin and hen egg white lysozyme (HEWL) were purchased from Sigma-Aldrich (St. Louis, MO, USA) and used without further purification. Thermolysin and hen egg white lysozyme (HEWL) were crystallized using a batch method (Allaire et al., 2009). HEWL was dissolved in 20 mM sodium acetate, pH 4.6, to a concentration of 70 mg/mL and mixed 1:1 with precipitant (20 mM sodium acetate, pH 4.6, 8% (w/v) sodium chloride, 10% (v/v) ethylene glycol) in a 15 mL conical tube. The sample was stirred continuously at room temperature for 24 hours. Thermolysin was dissolved in 50 mM sodium hydroxide to a concentration of 30 mg/mL and mixed 1:1 with 15% (w/v) ammonium sulfate in a 15 mL conical tube and stirred continuously at room temperature for 24 hours. Crystals of the 3.6 mega-Dalton extracellular hemoglobin from *G. paulistus* (oxy-HbGp) were grown in the hanging drop setup. Protein (18 mg/mL in 100 mM Tris-HCl, pH 7.5) was mixed with precipitant (1.6 M K_2HPO_4, pH 9.0) in a 1:1 ratio and equilibrated against an excess of the precipitant solution at room temperature (Ruggiero Bachega et al., 2015). Crystals typically appeared in 24-72 hours. Single crystals of oxy-HbGP are sensitive to X-ray irradiation, as noted by changes in the spectroscopic signal as a function of X-ray exposure (Andi *et al.*, *manuscript in*

preparation). These crystals typically exhibit nearly complete conversion of the electronic absorption spectroscopic features within approximately 100 kGray dose. Crystals of the giant extracellular hemoglobin were successfully injected into the LCLS X-ray beam, producing diffraction to 4.6 Å.

Crystals of diferrous Fe(II)-MauG in complex with quinol MADH (space group *C*2) were grown by hanging drop vapor diffusion in an anaerobic glovebox (Belle Technologies, UK) as described previously (Yukl et al., 2013). In brief, the protein sample contained 100 μM MauG, 50 μM MADH and 2 mM sodium dithionite in 10 mM potassium phosphate, pH 7.5. 3 μL of reservoir solution (22-26% (w/v) polyethylene glycol (PEG) 8000, 100 mM sodium acetate, 100 mM 2-(*N*-morpholino)ethanesulfonic acid, pH 6.4) were combined with 1 μL of protein solution. Plate-like microcrystals appeared after a few days. These were removed from the glovebox and allowed to air oxidize to diferric Fe(III)-MauG-quinone MADH. Just prior to data collection, H_2O_2 in crystal mother liquor was added to a final concentration of 2 mM to generate the *bis*-Fe(IV) state of the MauG in the MauG-MADH crystals (Li et al., 2008).

Crystals of PS II in PEG 2,000 were grown as previously reported (Kern et al., 2005) using a batch method. The protein solution (40 mg/mL in 100 mM piperazine-*N*,*N*'-bis(ethanesulfonic acid), pH 7.0, 5 mM $CaCl_2$, 0.03% β-dodecyl maltoside) was mixed 1:1 with 8% (w/v) PEG 2000 in 100 mM piperazine-*N*,*N*'-bis(ethanesulfonic acid), pH 7.0, 5 mM $CaCl_2$. Crystals formed within 3-5 days and were harvested using 10% (w/v) PEG 2000 in 100 mM piperazine-*N*,*N*'-bis(ethanesulfonic acid), pH 7.0, 5 mM $CaCl_2$. The same buffer was used for injection of the crystals. Crystals of PS II with PEG 5000 were grown as reported (Hellmich et al., 2014) using octaethyleneglycolmonododecylether ($C_{12}E_8$) instead of dodecyl maltoside as detergent by mixing the protein solution (20 mg/mL in 0.02 M MES (pH 6.0), 0.01 M $CaCl_2$ and 0.013 % $C_{12}E_8$) 1:1 with the precipitant solution (0.1 M TRIS, pH 7.5, 0.1 M $(NH_4)_2SO_4$, 15-18 % PEG 5000 MME (mono methylether). Crystals formed within 3 days and were harvested using 0.1 M TRIS, pH 7.5, 0.1 M $(NH_4)_2SO_4$, 10 % PEG 5000 MME and then stepwise transferred into the same buffer containing 40% PEG 5000 MME which was also used for injection of the crystals.

Crystals of aerobically purified or anaerobically purified Stc2 in complex with stachydrine (*N*,*N*-dimethylproline) and aerobically purified Stc2 were obtained as previously reported (Daughtry et al., 2012).

All crystal samples were either in their original mother liquor or in a few cases the mother liquor was supplemented with 0.08-0.2 % (w/v) agarose to counter crystal settling in mother liquor. In this concentration regime, agarose behaves as a Bingham fluid, suspending crystals in a solid-like gel matrix until sufficient force (from acoustic energy in this case) is applied to transform temporarily the mixture into a liquid (Biertumpfel et al., 2002; Sauter et al., 2009). Agarose-treated samples tended to maintain a homogenous distribution of crystals throughout the suspension for longer periods of time. For example, a thermolysin crystal slurry with agarose maintained a 15% crystal hit ratio (204 hits) sustained over 1331 shots. A nearly identical sample without agarose saw a significantly diminished crystal hit ratio after only 230 shots. Thus, the Bingham fluid can be an important additive for maintaining crystal ejection upwards out of a well.

Acoustic injector designs. Two acoustic injectors were used for crystal-containing droplet injection. The first was a modified Echo® 555, in which the acoustic transducer assembly and water bubbling column were placed external to the systems controls. The transducer ejects droplets with a fixed volume of 2.5 nL. The Echo 555 includes "Dynamic Fluid Analysis," a continuous, homeostatic process that determines the initial focus and acoustic power parameters and maintains it as the source fluid volumes decrease due to ejection. It also automatically adjusts for changes in fluid viscosity, attenuation of acoustic energy, and surface tension. Flowing water was used to acoustically couple the transducer in the modified Echo system to the well bottom and to maintain temperature stability. Control of the modified Echo 555 was accomplished by providing a TTL trigger signal from the LCLS to the Echo® software controllers.

The second acoustic injector is based on an acoustic reagent multispotter (Aerni et al., 2005). This device consists of an arbitrary waveform generator (Tabor Electronics, Tel Hanan, Israel), a

150 Watt broadband radiofrequency (rf) amplifier (Amplifier Research, Souderton, PA, USA), and several spot-focused piezoelectric transducers (Olympus NDT, Waltham, MA, USA) with center frequencies at 10, 15, and 25 MHz. The choice of transducer was based on the distribution of crystal sizes for a given sample. In the case of crystals smaller than ~50 μm, the 25 MHz transducer was chosen. For larger crystals up to 150 μm, the 15 MHz was used. For samples composed mostly of crystals larger than 150 μm, the 10 MHz transducer was used. Each transducer was excited at its peak frequency by a sine wave pulse of 60-400 μs duration. Signal amplitude was controlled through the waveform generator and the rf amplifier, and was varied along with the sine pulse duration to produce 20mW RMS per burst. Acoustic coupling was accomplished using either a 20 mm (for the 10 and 15 MHz transducers) or a 6 mm tall column of boiled and cooled 0.5 - 1% (w/v) agarose. We found these plugs to be robust, reliable, and did not impact injection accuracy; but, they do need to be kept well-hydrated between uses. Control of this acoustic injector was accomplished using a TTL trigger signal similar to the one used for the modified Echo® 555. During the experiment the waveform characteristics were monitored with a digital oscilloscope using an inline 30 dB dual directional coupler (Werlatone, Patterson, New York) placed between the amplifier and the transducer.

The droplets launched from the modified Echo were either obliterated by the X-ray pulse, evaporated, or fell down to an unknown location. The droplets from the inverted injector that were not destroyed were caught on a cover slip above a telescopic video camera

When ejecting slurries of protein crystals in their mother liquor, we have observed that the morphology and relative size of the particles can influence droplet trajectory. This is consistent with a large crystal, representing a substantial fraction of the droplet diameter, that perturbs the formation and break-off process of the droplet. Droplets containing rod- or plate-shaped crystals, for example, tend to exhibit deviations within the path from one drop to the next, causing some droplets to miss the interaction region if it is more than a few millimeters from the meniscus. One way to mitigate this effect is by increasing the size of the droplet relative to the crystal, at the expense of increasing background scatter from the droplet. For instance, in some cases we used a lower frequency transducer (11.5 or 15 MHz rather than 25 MHz) with the inverted system to inject larger droplets from slurries containing smaller average crystal size.

Given the fixed volume (2.5 nL, 11.5 MHz transducer) and diameter (roughly 168 μm) of each droplet generated by the modified Echo system, samples containing anisodiametric crystals were partitioned by size, with those crystals from 50-150 μm in diameter chosen for injection. The inverted system offered the capability to change the transducer frequency between runs, making it unnecessary to partition crystal samples based on size.

Our analysis of 6 mm flight trajectories of various solvents yields an average angular variation of 0.08° to produce deviations in X and Y of approximately 8 μm, which is similar to commercial applications (Ellson et al., 2003; Harris et al., 2008). An analysis of ejection events from which 40 ejections contained one 40 μm lysozyme crystal per 170 μm diameter drop from a slurry traveling 3.7 mm upward, yields an 82 ± 43 μm positional variance resulting from an approximate 1.2 ± 0.66° angular deviation in trajectory (see below, Estimating crystal ejection trajectory). We estimated the attenuation of the acoustic energy by the crystal slurry by comparison to the typical attenuation observed for scattering from monodisperse silica spheres in water (Povey, 2006). Assuming an average of one 40 μm crystal per two drops, where the crystal size is roughly half the drop size and corresponds to a suspension of ~6.2% v/v, this produces an acoustic attenuation of about 1.5 dB/mm by the crystal suspension.

XPP instrument setup and data collection. Experiments were carried out at room temperature and atmosphere at the XPP instrument at the LCLS. Injection of the samples into the interaction region was achieved by positioning a trimmed section of an acoustically compatible 384-well sample plate (Labcyte Inc., Sunnyvale, CA) directly below (Echo® instrument) or above (inverted setup) the interaction region. The sample well was overfilled to allow for visualization of the sample meniscus by the in-line camera. The sample meniscus was maintained 3-14 mm from the interaction region during droplet ejection. Droplets of crystals contained in their precipitant buffer (with and without agarose) were ejected at a rate of 0.4-120 Hz, which was controlled by the X-ray pulse scheme.

The XPP instrument was operated at an energy of ~9.1 keV with an average pulse energy of 1 mJ delivered to the sample, with a repetition rate of 0.4-120 Hz, and a pulse duration of 40 fs. The beam was focused down to a range between 20 x 20 μm and 100 x 100 μm in size FWHM

using compound refractive beryllium lenses. Forward diffraction was measured using the Cornell-SLAC Pixel Array Detector, which has fixed tiles containing approximately 2.3 million pixels (110 x 110 μm pixel size) (Hart et al., 2012).

The XPP compound refractive X-ray lenses (CRL) used for the experiment were focused to various distances behind the sample interaction region in order to achieve larger beam spots at the sample position than the smallest CRL focus (~2 μm; Rayleigh length at sample position 10 mm). The exact focal length of different combinations of CRL lenses used at XPP generally shows to be within a few cm from the calculated position. Working out-of-focus, this uncertainty relates to 100 ± 5 μm, 60 ± 6 μm, 30 ± 6 μm for the worst case scenario assuming a 50 mm deviation from calculation. Because the crystal sizes varied more than those uncertainties, we relied on the calculations together with beam size estimates observed with a fluorescent screen brought to the sample location as part of the motorized setup and viewed on-axis by a short focal length microscope. This microscope was also used to bring the droplets into the referenced beam position by adjusting the position of the drop injector, as well as the timing of the drop injection trigger, to a precision of about 20 % of the typical crystal dimension. The droplet position was observed throughout operation and corrected in case of drifts from the referenced beam position. A transmissive, single-shot X-ray spectrometer was positioned further upstream of the aperture to record spectral information from each pulse (Zhu et al., 2012). Other beamline components included a stroboscopic on-axis camera system for capturing droplet ejection events and a beamstop placed immediately downstream of the interaction region.

Data processing and refinement. All diffraction data were processed using *cctbx.xfel* (Hattne et al., 2014) as well as with a new version of *cctbx.xfel*, to improve the indexing and integration of our SFX diffraction datasets (Sauter, 2015; Sauter et al., 2014). Most importantly, the new code uses a maximum-likelihood target function for calculating the mosaicity. It corrects the previous code by including all the observations, and leads to a smaller mosaicity value that more closely conforms to the actual observed spots. When coupled with an improved arctan()-based function to calculate how far away a modeled reflection is from the Ewald

sphere, we are able to extract much more data from many of our SFX runs. All images were corrected for dark subtraction first, followed by background subtraction to remove noise due to water and air scatter. Additional features such as the beam stop shadow and, in some instances, the sample well shadow were masked out prior to indexing and integration. Individual reflections were scaled and merged without separately accounting for the partiality fraction of each observation. Integrated intensities were scaled to intensities derived from an isomorphous reference structure (PDB codes 3VCP for Stc2, 4ET8 for lysozyme, and 2TLI for thermolysin) in order to correct for variations in crystal size and pulse power (Hattne et al., 2014). Droplet hit ratios were calculated as the sum of crystal hits (as determined by *cctbx.spotfinder* (Zhang et al., 2006)) plus images containing water scatter (**Fig. S2A**). Three merged SFX datasets (Stc2, lysozyme, and thermolysin) were refined through several cycles of maximum likelihood refinement in Refmac 5.8.0069 (**Tables S2 – S4**). An example of the electron density for the lysozyme structure is shown in **Figure S3**.

Detecting diffuse water scattering. Droplet hit rates were calculated as the sum of the number of images with greater than 15 or more Bragg peaks and the number of images containing diffuse water scatter at 3.1Å. For images not containing Bragg peaks, diffuse water scatter was detected by first calculating the radial average intensity of each image (**Fig. S2A**). From the radial average intensity, the natural log of the intensity against the natural log of the scattering vector was analyzed using a least squares binomial regression. An *F*-observed value below 10,000 was used as a cutoff for water scatter.

Analysis of Bragg peak spread. 17,356 Bragg peaks were indexed from 479 lysozyme images. Of those, 3,649 reflections (21%) were recorded on a single pixel (**Fig. S2B**). These low mosaic spread images would be challenging for data processing routines—including those specially designed for processing FEL data—that typically reject single pixels whose intensities deviate substantially from local background (Sauter et al., 2013; White et al., 2013). Indeed, applying a one-pixel filter to this subset of data causes almost half of the images to fail during indexing. Development is underway to modify the current SFX data processing software to provide better estimates of Bragg peak profiles from low mosaicity samples.

Droplet formation for semi-dilute viscoelastic solutions. Delayed droplet fission is often a result of increased viscoelasticity in polymer-containing solutions (Cooper-White et al., 2002; Tirtaatmadja et al., 2006; Yan et al., 2011). Instead of droplets pinching off according to Newtonian theory an elongated column of liquid forms. This phenomenon manifests at concentrations in the dilute and very dilute regimes, and intensifies systematically up to the coil overlap concentration. At concentrations above the coil overlap concentration other effects such as partial alignment and entanglement between individual polymer molecules will contribute to delayed droplet pinch-off, complicating the behavior of droplet formation. Delayed droplet fission has been observed in samples containing polymers such as polyethylene oxide and polyethylene glycol (PEG), as well as denatured genomic DNA.

Delayed droplet fission was observed in several samples containing PEG polymers above the theoretical coil overlap concentration. In the case of PS II crystals that were acoustically injected from solutions containing up to 10% (w/v) PEG 2,000 or up to 40% (w/v) PEG 5,000, droplets would often not begin to break off until the liquid column was 5-6 mm long. MauG samples in solutions containing up to 30% (w/v) PEG 8,000 likewise exhibited delayed droplet formation. Conversely, Stc2 samples containing 2.5% (w/v) PEG 3,350 did not display significant column elongation compared to non-viscoelastic samples such as lysozyme.

Some viscous Mother Liquor conditions (e.g. >20% PEG 8000) yield extended columns, within which we observed crystals measuring tens of microns circulating through the extensions in the inverted setup. When the X-ray beam is aligned to this extended region, then the one has an opportunity to recycle unexposed samples during the particular data collection run. However, this also raises the possibility that a given crystal may be exposed to more than one X-ray pulse through random circulation patterns, provided that the original pulse did not destroy the sample.

Estimating crystal ejection trajectory. A monodisperse 40 μm lysozyme crystal slurry (~ 12% v/v, crystals were dyed blue for contrast) was prepared and suspended in 0.15% agarose

and 20% glycerol-augmented mother liquor such that on average every other ejected drop contained at least one crystal. A turntable was constructed to rotate a printed "bull's eye" grid at a constant speed and served as the target and destination plate inside a commercial Echo 550. The Echo was programmed to eject at 500 drops/s, with a distance between the source plate and the destination turntable of 3.7 mm. 768 drops were ejected, of which 40 drops contained only one 40 μm crystal as determined by visualization with a light microscope. The distance between the center of these drops and the target position was 82 ± 43 μm, corresponding to an angular deviation in trajectory of 1.3° ± 0.66°. The angular deviation as the drop is ejected is very difficult to measure in real time. It does manifest as a displacement cone on the target with a height (distance traveled) that magnifies the impact of the angular variability.

Accession Numbers

Structure factors and atomic coordinates have been deposited with the PDB with the following IDs: Lysozyme (5F81), Stachydrine demethylase (5HL4) and Thermolysin (5HQD).

Supplemental References

Aerni, H.-R., Cornett, D.S., and Caprioli, R.M. (2005). Automated acoustic matrix deposition for MALDI sample preparation. Anal Chem *78*, 827-834.

Agustinho, S.C., Tinto, M.H., Imasato, H., Tominaga, T.T., Perussi, J.R., and Tabak, M. (1996). Spectroscopic studies of the met form of the extracellular hemoglobin from Glossoscolex paulistus. Biochim Biophys Acta *1298*, 148-158.

Allaire, M., Moiseeva, N., Botez, C.E., Engel, M.A., and Stephens, P.W. (2009). On the possibility of using polycrystalline material in the development of structure-based generic assays. Acta Crystallogr D Biol Crystallogr *65*, 379-382.

Bachega, J.F., Bleicher, L., Horjales, E.R., Santiago, P.S., Garratt, R.C., and Tabak, M. (2011). Crystallization and preliminary structural analysis of the giant haemoglobin from *Glossoscolex paulistus* at 3.2 A. J Synchrotron Rad *18*, 24-28.

Biertumpfel, C., Basquin, J., Suck, D., and Sauter, C. (2002). Crystallization of biological macromolecules using agarose gel. Acta Crystallographica Section D *58*, 1657-1659.

Cooper-White, J.J., Fagan, J.E., Tirtaatmadja, V., Lester, D.R., and Boger, D.V. (2002). Drop formation dynamics of constant low-viscosity, elastic fluids. J Non-Newtonian Fluid Mechanics *106*, 29-59.

Daughtry, K.D., Xiao, Y., Stoner-Ma, D., Cho, E., Orville, A.M., Liu, P., and Allen, K.N. (2012). Quaternary ammonium oxidative demethylation: X-ray crystallographic, resonance Raman, and UV-visible spectroscopic analysis of a Rieske-type demethylase. J Am Chem Soc *134*, 2823-2834.

Davidson, V.L. (1990). Methylamine dehydrogenases from methylotrophic bacteria. Methods in Enzymology *188*, 241-246.

Ellson, R., Mutz, M., Browning, B., Lee, L., Miller, M.F., and Papen, R. (2003). Transfer of low nanoliter volumes between microwell plates using focused acoustics – Automation considerations. J Assoc Lab Automation *8*, 29-34.

Harris, D., Mutz, M., Sonntag, M., Stearns, R., Shieh, J., Pickett, S., Ellson, R., and Olechno, J. (2008). Low Nanoliter Acoustic Transfer of Aqueous Fluids with High Precision and Accuracy of Volume Transfer and Positional Placement. Journal of the Association for Laboratory Automation *13*, 97-102.

Hart, P., Boutet, S., Carini, G., Dubrovin, M., Duda, B., Fritz, D., Haller, G., Herbst, R., Herrmann, S., Kenney, C., *et al.* (2012). The CSPAD megapixel x-ray camera at LCLS. Proc SPIE *8504*, 85040C.

Hattne, J., Echols, N., Tran, R., Kern, J., Gildea, R.J., Brewster, A.S., Alonso-Mori, R., Glockner, C., Hellmich, J., Laksmono, H., *et al.* (2014). Accurate macromolecular structures using minimal measurements from X-ray free-electron lasers. Nat Methods *11*, 545-548.

Hellmich, J., Bommer, M., Burkhardt, A., Ibrahim, M., Kern, J., Meents, A., Muh, F., Dobbek, H., and Zouni, A. (2014). Native-like photosystem II superstructure at 2.44 A resolution through detergent extraction from the protein crystal. Structure *22*, 1607-1615.

Kern, J., Loll, B., Lüneberg, C., DiFiore, D., Biesiadka, J., Irrgang, K.D., and Zouni, A. (2005). Purification, characterisation and crystallisation of photosystem II from *Thermosynechococcus elongatus* cultivated in a new type of photobioreactor. Biochimica et Biophysica Acta - Bioenergetics *1706*, 147-157.

Li, X., Fu, R., Lee, S., Krebs, C., Davidson, V.L., and Liu, A. (2008). A catalytic di-heme bis-Fe(IV) intermediate, alternative to an Fe(IV)=O porphyrin radical. Proc Natl Acad Sci USA *105*, 8597-8600.

Povey, M.J.W. (2006). Acoustic Methods for Particle Characterisation. KONA Powder and Particle Journal *24*, 126-133.

Royer, W.E., Jr., Sharma, H., Strand, K., Knapp, J.E., and Bhyravbhatla, B. (2006). Lumbricus erythrocruorin at 3.5 A resolution: architecture of a megadalton respiratory complex. Structure *14*, 1167-1177.

Ruggiero Bachega, J.F., Vasconcelos Maluf, F., Andi, B., D'Muniz Pereira, H., Falsarella Carazzollea, M., Orville, A.M., Tabak, M., Brandao-Neto, J., Garratt, R.C., and Horjales Reboredo, E. (2015). The structure of the giant haemoglobin from Glossoscolex paulistus. Acta Crystallogr D Biol Crystallogr *71*, 1257-1271.

Sauter, C., Balg, C., Moreno, A., Dhouib, K., Theobald-Dietrich, A., Chenevert, R., Giege, R., and Lorber, B. (2009). Agarose gel facilitates enzyme crystal soaking with a ligand analog. Journal of Applied Crystallography *42*, 279-283.

Sauter, N.K. (2015). XFEL diffraction: developing processing methods to optimize data quality. J Synchrotron Radiat *22*, 239-248.

Sauter, N.K., Hattne, J., Brewster, A.S., Echols, N., Zwart, P.H., and Adams, P.D. (2014). Improved crystal orientation and physical properties from single-shot XFEL stills. Acta Crystallogr D Biol Crystallogr *70*, 3299-3309.

Sauter, N.K., Hattne, J., Grosse-Kunstleve, R.W., and Echols, N. (2013). New Python-based methods for data processing. Acta Crystallogr D Biol Crystallogr *69*, 1274-1282.

Tirtaatmadja, V., McKinley, G.H., and Cooper-White, J.J. (2006). Drop formation and breakup of low viscosity elastic fluids: Effects of molecular weight and concentration. Physics of Fluids (1994-present) *18*, 043101.

Wang, Y., Graichen, M.E., Liu, A., Pearson, A.R., Wilmot, C.M., and Davidson, V.L. (2003). MauG, a Novel Diheme Protein Required for Tryptophan Tryptophylquinone Biogenesis. Biochemistry *42*, 7318-7325.

White, T.A., Barty, A., Stellato, F., Holton, J.M., Kirian, R.A., Zatsepin, N.A., and Chapman, H.N. (2013). Crystallographic data processing for free-electron laser sources. Acta Crystallogr D Biol Crystallogr *69*, 1231-1240.

Yan, X., Carr, W.W., and Dong, H. (2011). Drop-on-demand drop formation of polyethylene oxide solutions. Physics of Fluids (1994-present) *23*, 107101.

Yukl, E.T., Jensen, L.M., Davidson, V.L., and Wilmot, C.M. (2013). Structures of MauG in complex with quinol and quinone MADH. Acta Crystallogr F *69*, 738-743.

Zhang, Z., Sauter, N.K., van den Bedem, H., Snell, G., and Deacon, A.M. (2006). Automated diffraction image analysis and spot searching for high-throughput crystal screening. Journal of Applied Crystallography *39*, 112-119.

Zhu, D., Cammarata, M., Feldkamp, J.M., Fritz, D.M., Hastings, J.B., Lee, S., Lemke, H.T., Robert, A., Turner, J.L., and Feng, Y. (2012). A single-shot transmissive spectrometer for hard X-ray free electron lasers. Appl Phys Lett *101*, 034103.